Pergamon

Int. J. Solids Structures Vol. 32, No. 17/18, pp. 2779–2791, 1995

0020–7683/95 $9.50 + .00

0020–7683(94)00297–5

EXPERIMENTAL MEASUREMENT OF DYNAMIC FAILURE AND FRAGMENTATION PROPERTIES OF METALS†

D. E. GRADY and M. E. KIPP
Sandia National Laboratories, Albuquerque, NM 87185, U.S.A.

(*Received* 3 *February* 1994)

Abstract—An experimental method for determining failure and fragmentation properties of metals in catastrophic breakup events has been pursued in this work. Spherical samples of the test metals were launched at high velocities with a two-stage light-gas gun facility and subjected to controlled impulsive loading by impact on a stationary non-metallic plate. Fragmentation and motion of the debris were diagnosed with multiple flash radiography. Methods for determining critical failure properties and the fragmentation toughness of the test metals were explored.

1. INTRODUCTION

Some basic theories have emerged within the past 10 years for predicting the consequences of dynamic fragmentation brought about by high-velocity impact or explosive events. These theories have focused principally on the prediction of mean fragment size through energy and momentum balance principals [e.g. Grady (1982, 1988); Kipp and Grady (1985); Glenn and Chudnovsky (1986)], and on the statistical issues of fragment size distributions [e.g. Englman *et al.* (1984); Grady and Kipp (1985); Brown (1989); Grady (1990)]. These theoretical bases provide the underlying framework for a number of computational algorithms employed to analyze complex fragmentation events [e.g. Smith (1989); Johnson *et al.* (1990); Melosh *et al.* (1992); Kipp *et al.* (1993)].

There are, nonetheless, a number of unresolved issues within the development of statistical energy-balance theories of fragmentation, and there is a pressing need for high-resolution experimental data focused on the validation of these theories. Furthermore, implementation and validation of these theories in Eulerian wave propagation codes are needed for the investigation of dynamic fragmentation in complex large scale catastrophic events.

A critical issue is a need for material property data for solids of interest which characterize the failure and fragmentation behavior under intense stress-wave loading. Although static fracture data frequently exist for these materials, the current state of theoretical understanding does not provide for the confident extension of these data into the highly dynamic regime.

In the present study we explore the possibilities of using a newly developed impact fracture and fragmentation experiment to determine dynamic failure and fragmentation properties of metals. A sample of the test material is prepared in the form of a solid sphere and launched with a light-gas gun facility. The test sphere is caused to impact a thin plate of low-density non-metallic material and to undergo catastrophic fragmentation. Flash radiography is used to image the fragmented specimen at several stations. Only the metal debris is imaged on the radiograph because of the low density of the impact plate material. From the extent of fragmentation and velocity of debris expansion, fragmentation properties of the metal are inferred. In subsequent sections exploratory studies and the development of this work are described.

† This work was performed at Sandia National Laboratories supported by the U.S. Department of Energy under contract number DE-AC04-94AL85000.

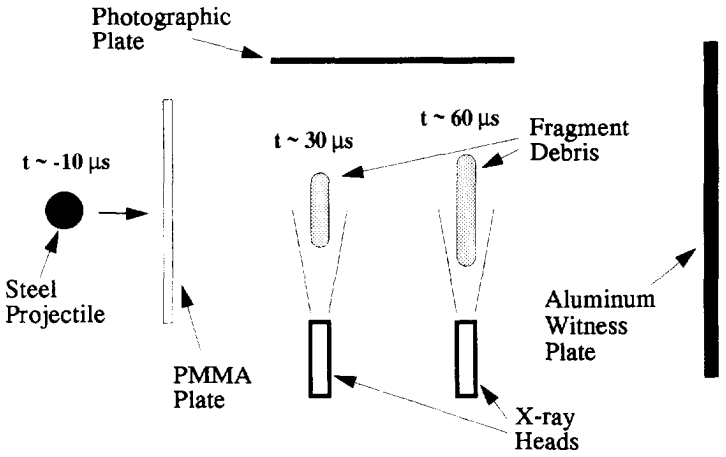

Fig. 1. Experimental configuration for radiographic and witness plate diagnostic of impact fragmentation experiment (timing is representative of a 5 km s^{-1} impact).

2. EXPERIMENTAL METHODS AND MATERIALS

The experimental configuration for investigating the fragmentation properties of metals is shown in Fig. 1. Solid metal spheres mounted in lexan sabots were launched at velocities between about 3 and 5 km s^{-1} with a two-stage light-gas gun system. The diameter of the launch tube used was 12 mm. Plastic sabots were separated from the metal spheres through forces produced by a rarefied atmosphere in the gun range section. Sabot segments were trapped upstream and did not reach the target impact chamber. Velocity of the metal spheres was measured to $\pm 1\%$ accuracy by recording of the time interval during passage between two magnetic coils of known separation. Normal impact occurred in the target chamber at the center of a 75×75 mm square plastic target plate of thickness between 0.6 and 11 mm. The plastic was polymethylmethacrylate (PMMA) Rohm and Haas Type II UVA, and had a normal density of 1186 kg m^{-3}.

In this exploratory series of experiments, steel spheres 6.35 mm ($\frac{1}{4}$ in) in diameter were used. The measured mass was 1.027 ± 0.001 g. The steel examined in this initial study was AISI E52100 high-carbon chromium steel, heat treated to a Rockwell-C hardness of 60–67. The density of the steel was 7837 kg m^{-3}, static yield strength was 2.03 GPa, fracture toughness was 30–40 MPa $m^{1/2}$ and bulk elastic modulus was 164 GPa, with a Poisson ratio of 0.29.

Fragment debris was diagnosed at two stations (approximately 150 and 300 mm) downstream from the input point. Two 150 keV flash X-ray tubes, placed approximately 400 mm from the line of debris travel, provided orthogonal shadow-graphs of the fragment debris, as shown in Fig. 1. Appropriate delay times were calculated from the predicted impact velocity and the X-ray tubes were independently triggered from the second magnetic velocity coil. The X-ray film cassette, using Kodak Direct Exposure film backed by a Quanta Fast Detail screen, was stationed about 100 mm from the centerline of the debris trajectory. The fragment debris impacted an aluminum witness plate which provided an independent measure of particle size and velocity statistics (Kipp, 1993).

3. EXPERIMENTAL RESULTS AND EVALUATION

In the present study, 24 experiments were performed to investigate the modes of dynamic fragmentation and the variations brought about by changes in impact velocity and the thickness of the PMMA plate. One example of an experimental radiograph is shown in Fig. 2(a), illustrating qualitatively the nature of the fragmentation process observed in all of the tests with the exception of several tests in which parameter extremes (highest velocities or thickest impact plates) were reached. As seen in the radiograph, the steel fragments remained well grouped and continued to move along the original trajectory at velocities somewhat less than the initial impact velocity, having been slowed by the impulse

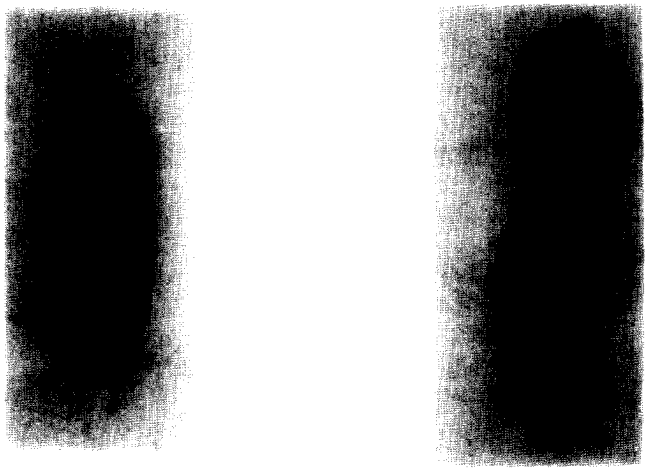

(a)

(b)

Fig. 2. (a) Radiographic images from test 5 illustrating the general fragmentation character observed in the majority of experiments in the present study. The time interval between images is 33.2 μs. Diameter of the debris disc is about 28 mm in the first X-ray and 46 mm in the second. (b) Oblique X-ray radiograph from test 2. Debris is imaged from behind, 30.5° from the perpendicular. The vertical extent of the debris is about 45 mm.

Table 1. Experimental impact parameters and debris properties

Test number	h (mm)	V_i (m s^{-1})	ΔV (m s^{-1})	V_e (m s^{-1})	Test number	h (mm)	V_i (m s^{-1})	ΔV (m s^{-1})	V_e (m s^{-1})
1	3.28	4460	†	†	13	5.37	4430	460	290
2	3.28	4460	†	†	14	5.36	4060	330	183
3	1.74	4450	—	200	15	5.38	3310	240	50
4	1.74	4700	150	147	16	5.37	4080	330	164
5	3.38	4570	270	271	17	3.25	4520	195	223
6	3.28	3460	200	52	18	4.71	4430	345	219
7	3.44	4160	250	171	19	5.39	4610	410	660‡
8	1.49	3950	130	105	20	4.75	4040	295	158
9	1.51	3460	170	44	21	4.78	3750	270	82
10	0.63	3410	50	0	22	0.99	4700	85	72
11	0.64	3920	60	0	23	11.23	4060	785	580‡
12	0.69	4470	90	0	24	9.47	4030	680	540‡

† Oblique impact experiments.
‡ High-velocity umbrella spray (see text).

delivered to the sphere by the plate. Axial dispersion of the fragment debris was quite limited, with fairly well-defined, nearly planar boundaries forming. Radial dispersion was significant, however, although the fragments were constrained within rather well-defined limits. Off-normal radiographic experiments, illustrated in Fig. 2(b), were performed which demonstrated fairly uniform diametral distribution in both fragment density and size. These observations held in general except for the very largest of target thicknesses. Since the PMMA was not recorded in the radiograph, we are assured that only the mass of the original steel sphere is represented in each image. The primary experimental parameters for all tests performed in the present study are provided in the first two columns of Table 1, where h is the PMMA plate thickness and V_i is the impact velocity.

The nature of the fragmentation process in the present tests can be described within the framework of Fig. 3. Points identify the impact velocity and target plate thickness on the vertical and horizontal axes, respectively. The product of the two parameters provides an approximate measure of the impulse imparted to the steel sphere. Solid curves in Fig. 3 are then constant curves of this product. The fragment pattern for all tests in region II approximated that shown in Fig. 2. For those tests in region II with plate thicknesses less than approximately 2.5 mm (vertical dashed line in Fig. 3) there was a tendency to separate into two clouds of fragment debris suggesting an axial spall plane in the sphere interior. Over a relatively broad range of plate thicknesses (3–6 mm) a uniform and self-similar disc of fragment debris was produced. For very thin plates (region I) in the present velocity range the impulse was insufficient to cause breakup. For quite thick plates and also for one

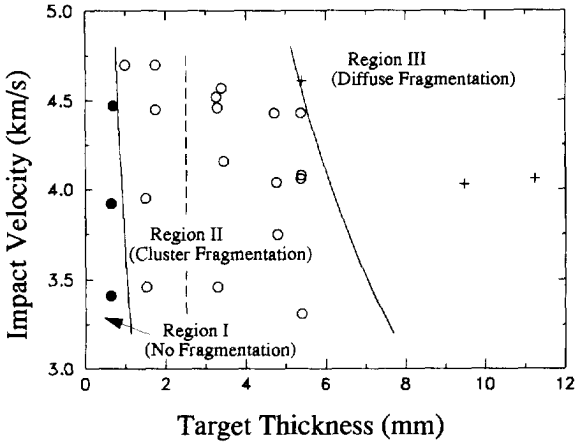

Fig. 3. Plot of impact velocity versus target thickness. Different regions of fragment debris characteristics are identified and separated by iso-impulsive curves. The vertical dashed line separates distinct fragment pattern differences in region II (see text).

test at the highest impact velocity on a 6 mm plate (region III) transition to a behavior in which a trailing umbrella pattern of high-radial-velocity fine fragment debris was observed (tests 19, 23, 24). This region of behavior was identified as diffuse fragmentation and conditions leading to its onset are not well understood. For the present purpose of determining fragmentation properties, interest will focus on the region II behavior (self-similar disc of fragment debris), and this mode of breakup will be examined further.

It is apparent from the radiograph in Fig. 2 that the impulse imparted to the steel sphere by the PMMA plate will redistribute the initial kinetic energy of the steel sphere into kinetic energies of axial translation and radial expansion of the steel fragments, kinetic energy of the PMMA debris and energy expended in the various dissipative processes active during the impact process. The axial velocity change, ΔV, recorded for the experimental series in Table 1, provides a measure of the translational momentum loss by the steel sphere upon impact. These results are plotted against the product of the PMMA plate thickness and the steel sphere impact velocity, hV_i, in Fig. 4. As noted earlier, this latter parameter provides a measure of the impulse delivered to the sphere by the PMMA target. Within experimental scatter, the ΔV data are found to be single-valued functions of the parameter hV_i.

The trend of the data in Fig. 4 can be reasonably well understood in terms of a relatively basic hydrodynamic description of the sphere and target interaction [e.g. Backman and Goldsmith (1978)]. The deceleration of the steel sphere of mass m can be determined from

$$m\frac{\mathrm{d}V}{\mathrm{d}t} = -\tfrac{1}{2}\rho V^2 A, \tag{1}$$

where $\rho V^2/2$ is the Bernoulli pressure applied by the PMMA target material, of density ρ, under steady flow conditions, and is assumed to apply over the projected geometric area A of the sphere. For target plate thicknesses h of the order of the sphere diameter or less, a first order solution of eqn (1) provides the functional relationship of the decrease in velocity with the impact velocity and target thickness,

$$\Delta V = \frac{\rho A}{2m} hV_i. \tag{2}$$

Comparison of eqn (2) with the measured velocity decrease, tabulated in Table 1, is shown in Fig. 4, and demonstrates reasonable agreement with this approximate analysis. A more complete development should look more carefully at the transient shock pressure which also tends toward a V^2 dependence in the present impact velocity range.

For the tests exhibiting region II behavior in which an expanding disc-shaped pattern of fragment debris was observed, radial expansion velocity data (see Table 1) are plotted

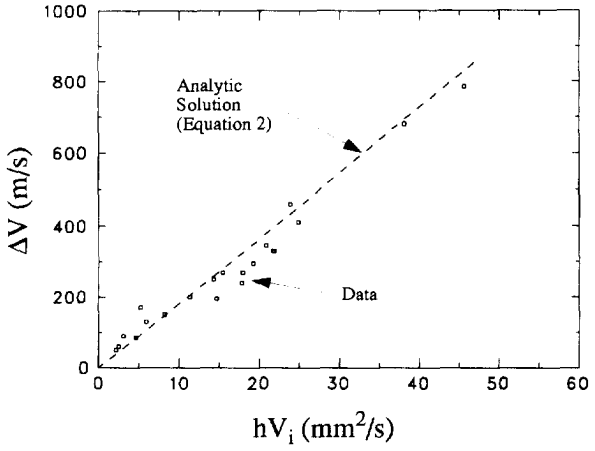

Fig. 4. Translational velocity reduction data. Dependence on product of target plate thickness and impact velocity.

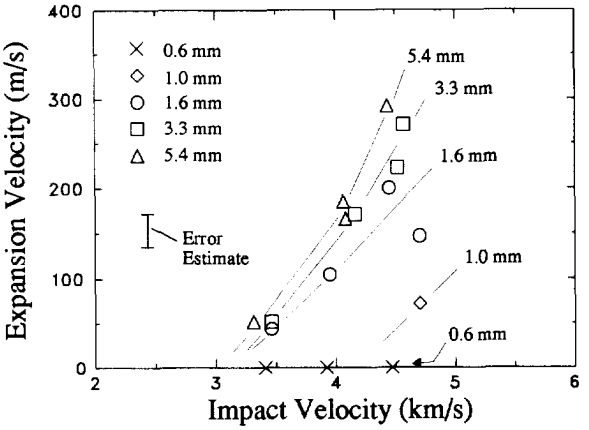

Fig. 5. Radial expansion velocity of fragment debris. Tests with nominally similar target-plate thicknesses are plotted against the impact velocity.

as functions of impact velocity and impact plate thickness, as shown in Figs 5 and 6. In Fig. 5, tests of nominally the same plate thickness are identified by a common symbol and plotted against the impact velocity. Although data scatter tends to obscure detailed trends, some clear observations emerge. First, at similar impact velocities, the expansion velocity initially increases with increased plate thickness but becomes nearly insensitive to plate thickness at larger plate thicknesses. This trend is most noticeable at the higher impact velocities. Second, there is a critical impact velocity below which fragmentation and subsequent fragment expansion do not occur. This velocity limit is outside the range of the data for the 0.6 mm plate. [A single small fragment was observed to spall off of the back of the steel sphere at the highest velocity (4470 m s^{-1}) experiment for the 0.69 mm plate.] The critical velocity is probably around 4000 m s^{-1} for a 1.0 mm plate. For thicker plates (1.6 mm and above) this critical velocity (about 3000 m s^{-1}) becomes independent of plate thickness, as found by extrapolating to zero expansion velocity in Fig. 5. In Fig. 6, an alternative representation of the expansion velocity data is shown. Expansion velocity is plotted against plate thickness at nominally similar impact velocities. Increased expansion velocity with increasing impact velocity is seen. Flattening of the curves for plate thicknesses above about 2 mm is clearly observed showing that the initial transient shock pressure, and not the sustained hydrodynamic pressure, is principally responsible for producing the radial impulse and expansion.

4. FAILURE ENERGY

The translational impulse imparted to the fragment debris appears to be a consequence of the momentum exchanged during hydrodynamic penetration of the target plate. This

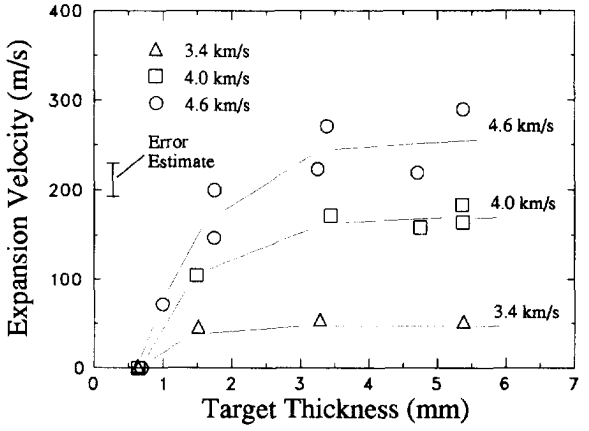

Fig. 6. Radial expansion velocity of fragment debris. Tests at nominally similar impact velocities are plotted against target plate thickness.

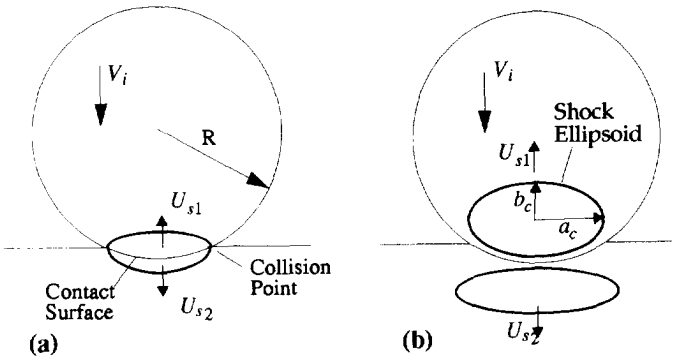

Fig. 7. Geometry of shock-wave coupling upon normal impact of a spherical particle on a planar surface.

conclusion is supported by the nearly linear dependence of the measured translational velocity change on plate thickness as seen in Fig. 4, in agreement with the analytic expression given in eqn (2). In contrast, the evidence displayed in Figs 5 and 6 suggests that the radial impulse acquired by the impacting sphere fragment debris is a consequence of the early shock phase of the interaction and is little affected by the later hydrodynamic penetration phase.

To pursue the shock energy coupling process we shall examine an analytic theory of the shock interaction event and compare implications with the observed trends in the expansion velocity data. Because of the spherical geometry of the impacting projectile, the coupling of shock energy into the projectile is transient and constrained to the central impact surface of the projectile. An analysis of the impact conditions due to Ang (1990) can be used to calculate duration and magnitude of the coupled shock energy.

Referring to the geometry illustrated in Fig. 7, for a spherical projectile undergoing normal impact at a velocity V_i on a planar surface, the distance of the collision point from the centerline at time t is

$$a = V_i t \sqrt{\left(\frac{2R}{V_i t} - 1\right)}. \tag{3}$$

The velocity of the collision point is provided by the derivative of eqn (3):

$$\dot{a} = \frac{V_i[(R/V_i t) - 1]}{\sqrt{[(2R/V_i t) - 1]}}. \tag{4}$$

The collision velocity is initially infinite and decreases with time. As curvature of the impacting sphere at the contact point increases, the collision velocity will continue to decrease [Fig. 7(a)], ultimately allowing a lateral release wave to propagate inward, quenching the shock coupling phase [Fig. 7(b)].

A reasonable assumption is that shock waves will couple into both materials over the lateral distance at which $\dot{a}$ reduces to the release wave velocity in the faster material. We shall approximate the release velocity by the shock velocity U_s in the faster material. (Release waves are dispersive but U_s is approximately equal to the release velocity at one-half of the Hugoniot particle velocity in a linear shock velocity–particle velocity material.) The time t_1 at which $\dot{a} = U_s$ is calculated from eqn (4) through:

$$U_s = \frac{V_i[(R/V_i t_1) - 1]}{\sqrt{[(2R/V_i t_1) - 1]}}. \tag{5}$$

The corresponding radius at this time is provided by eqn (3):

$$a_c = V_i t_1 \sqrt{\left(\frac{2R}{V_i t_1} - 1\right)}. \tag{6}$$

The release time t_2 is in turn calculated from the radius a_c and the release velocity (shock velocity U_s) in the faster material through,

$$t_2 = a_c/U_s. \tag{7}$$

The axial thickness b_c of the shock pulse in the sphere [see Fig. 7(b)] is then determined from

$$b_c = \tfrac{1}{2}U_{s1}(t_1 + t_2), \tag{8}$$

where U_{s1} is the shock velocity in the sphere material. A reasonable estimate of the region of shock coupling into the spherical projectile is an ellipsoidal volume with major axis a_c and minor axis b_c. Hence the coupled shock energy (kinetic and internal) is provided by the volume of material times its energy density:

$$E_s = \frac{4\pi}{3}a_c^2 b_c \frac{p_h^2}{\rho U_{s1}^2}. \tag{9}$$

The shock energy provided by eqn (9) is necessarily approximate due to the simplification needed to complete the analytic solution. Also, there is not a clear transition time between the transient shock and the quasi-steady hydrodynamic phases of the impact and penetration process. Nevertheless, comparisons of eqn (9) with wave-code simulations of spherical impact on planar surfaces (Kipp *et al.*, 1993) have shown reasonably close agreement (within about 25%).

A portion of the shock energy coupled into the projectile will be dissipated in shock heating. This heat energy is calculated to be about 10% of the shock energy at the present impact amplitudes. Momentum conservation requires that a portion of the shock energy also be converted into kinetic energy associated with axial motion. This energy is also about 10% of the total shock energy. Most of the shock energy will go into plastic distortion and fracture of the projectile, and radial kinetic energy of fragments if the impact is sufficiently intense.

Carrying through the analysis needed to calculate the shock energy from eqn (9) for a 4600 m s^{-1} impact velocity, and reducing this value by the required heat and axial kinetic energies, provides an energy available for radial expansion of about 33 J. If we assume that this energy is fully coupled into the uniform radial expansion of a uniform disc of fragment debris (kinetic energy = $mV_e^2/4$), an expansion velocity of V_e = 360 m s^{-1} is calculated. Comparison with the appropriate expansion data in Fig. 8 (see also Fig. 6) finds the calculated value somewhat higher than the data.

Although approximations in the analytic solution could probably encompass the observed difference between calculation and experiment, it is nevertheless worthwhile attempting to account for energy absorbed in the fragmentation process to assess the expected level of influence on the calculated expansion velocity. First, energy to create

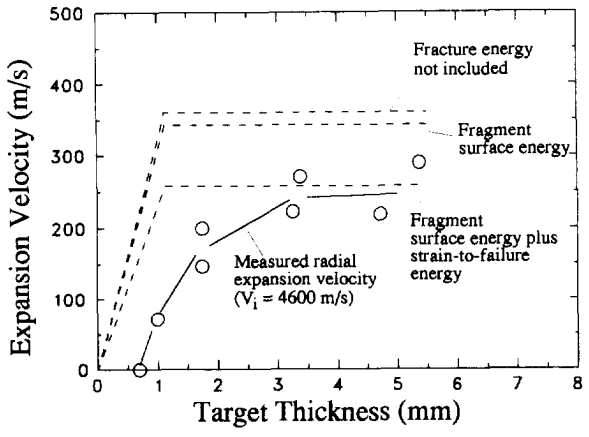

Fig. 8. Comparison of calculated and measured radial expansion velocities for debris fragments at 4600 m s^{-1} impact velocity.

fragment surface area can be expected to reduce the radial kinetic energy. Using a fracture toughness of $K_c = 35$ MPa $m^{1/2}$, a fracture surface energy from $\Gamma = K_c^2/2\rho c^2$ is calculated to be about 3800 J m^{-2}. At an impact velocity of 4600 m s^{-1} a total number of about 200 fragments is estimated from the radiographs. For this degree of fragmentation, a fragment surface energy of about 2.8 J is calculated. Reducing the 33 J expansion energy by this amount leads to a slightly lower expansion velocity of about $V_e = 343$m s^{-1} (see Fig. 8).

Static tensile tests on the present steel provide a strain to failure of $\varepsilon_f \approx 0.05$ (5%). Assuming a similar strain to failure under the dynamic conditions of the impact fracture process, a strain-to-failure energy, $E_f = Y\varepsilon_f$ ($Y = 2$ GPa is the yield stress), provides an additional fracture energy of 13.4 J. Accounting for both fracture surface energy and strain-to-failure energy further reduces the expansion velocity to about $V_e = 258$ m s^{-1}. It is worth noting from the radiographic record for test 12 that this projectile indicated a plastic distortion of about 5% without fragmentation.

As developed earlier, the transient shock energy is coupled into the spherical projectile in a time of $t_1 + t_2$ [see eqns (5)–(8)]. This time requires that the target plate be thicker than $U_{s2}(t_1 + t_2)/2$ where U_{s2} is the shock velocity in the target material. For an impact velocity of 4600 m s^{-1} this thickness is calculated to be approximately 1.1 mm. Thinner target plates would lead to reduced shock energies and radial expansion velocities as suggested by the linear decrease in predicted velocity for thicknesses below 1.1 mm in Fig. 8. In contrast, target plates thicker than 1.1 mm would not increase the coupled shock energy and the expansion velocity should be independent of increasing plate thickness. This predicted behavior approximates the observed behavior in Fig. 8.

5. THRESHOLD FAILURE PROPERTIES

At this point we shall begin to explore the experimental method as a technique for evaluating critical dynamic failure and fragmentation properties of the test metal. In Fig. 9 the expansion velocity data for the four tests with a nominal plate thickness of 3.3 mm are plotted. The data extrapolate to zero expansion velocity at an impact velocity of approximately 3100 m s^{-1}. The shock pressure at this threshold impact velocity is approximately 20.3 GPa. As noted earlier, this threshold velocity is relatively insensitive to plate thicknesses between about 1.6 and 5.4 mm (see Fig. 5).

It is reasonable to consider the use of this threshold impact velocity to extract experiment-independent failure properties of the test metal. At 3100 m s^{-1} the shock energy predicted from eqn (9) in the previous analysis is approximately 18 J. Ignoring the small corrections for shock heating and axial impulse this energy represents the energy the test metal is capable of absorbing without failure by dynamic fracture. It is most likely a

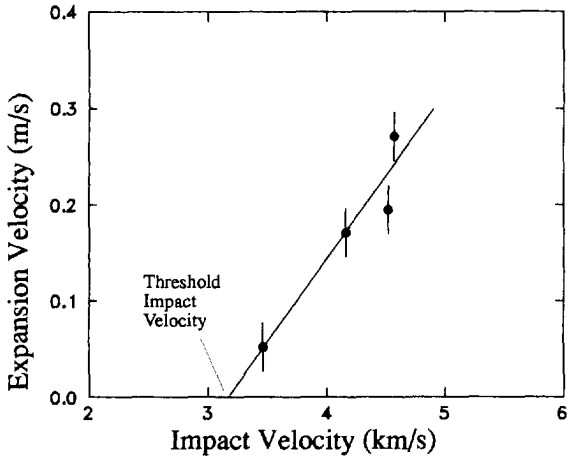

Fig. 9. Expansion velocity versus impact velocity for E51200 steel on nominal 3.3 mm PMMA plate thickness indicating threshold impact velocity.

measure of the plastic work sustained by the body prior to failure. The disc-shaped expansion imparted to the fragment debris in the present test method suggests that, although complex, strain-to-failure nominally occurs under a low confining-stress environment. This contrasts, for example, to a strain-to-failure occurring in a spall experiment in which a strong tensile confining-stress environment exists.

Dynamic energy-to-failure is the fundamental property determined in the present test. The unknown dynamic stress history precludes calculation of the strain-to-failure. If a static yield stress of 2 GPa for E52100 steel is assumed, a strain-to-failure of approximately 7% is calculated for the 18 J failure energy. More recent tests not described here suggest that an indication of the strain-to-failure can be obtained from radiographic data on sub-threshold impact tests.

6. FRAGMENTATION PROPERTIES

As is seen in the radiographic data in Fig. 2, an indication of the extent of fragmentation (fragment number or statistical fragment size) can be obtained, in addition to the kinematic state of the fragment debris. This data is difficult to extract from radiograph records, however, because of the overlap and shadowing of fragments which occur if sufficient spreading of the fragment debris is not allowed before X-ray imaging. The latter solution is often inconsistent with other objectives of the radiographic diagnostics. For example, preliminary examination of the images shown in Fig. 2 for test 5 indicates about 200 particles, with an average fragment size of about 1 mm and a largest fragment size of about 2 mm.

A useful method for extracting fragment number and average fragment size data from radiographs of reasonable tightly packed fragment debris clouds is based on a statistical formula for randomly positioned areas (Johnson and Mehl, 1939). The approach can be conceptualized by imagining coins of various sizes which are tossed and land at random positions on a table of a specified area A_{reg}. After N coins have been thrown the total area of interest A will be the sum of the areas of the N coins. The area of the table that is covered, however, will be less because of overlapping due to the random placement of the coins. If the area covered is A_{obs}, then the statistical theory leads to a relation between the observed area A_{obs} and the actual area A of the N coins randomly distributed on the region A_{reg}:

$$A = A_{obs} \ln (1-f)^{-1/f}, \tag{10}$$

where $f = A_{obs}/A_{reg}$ is the fraction of the region (table) covered by coins. A Taylor expansion of eqn (1)

$$A = A_{obs}\left(1 + \frac{f}{2} + \frac{f^2}{3} + \cdots\right) \tag{11}$$

reveals that A is always greater than A_{obs} and approaches A_{obs} as f becomes small.

Application of the statistical relation in eqn (10) or eqn (11) to radiographs of fragment debris is reasonably clear. Because of shadowing and overlap of fragments in the relatively dense debris cloud, the fragment area projected on the radiographic image will be less than the projected area of the same fragments if shadowing and overlap does not occur—the latter being the desired property. Thus, image processing of the radiographic record requires two measured properties, the total observed projected fragment area A_{obs} and an estimate of the area fraction of the debris cloud region masked by the debris fragments. Assuming a random distribution of fragments through the region, eqn (10) provides the required projected fragment area. Note that if f is reasonably small the expression for A is relatively insensitive to inaccuracies in f.

Knowing the total volume of fragmented material within the debris cloud, the number of fragments N and the average fragment size S are related through $V = NS^3$. In addition the total projected area satisfies $A = NS^2$. Solving these relations provides the average fragment size:

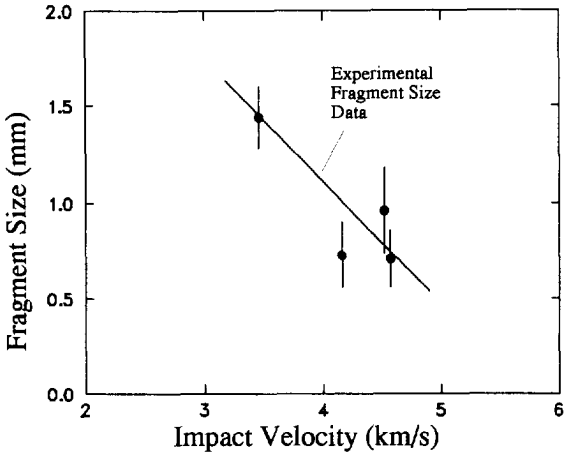

Fig. 10. Fragment size versus impact velocity for E51200 steel (Fig. 9 data).

$$S = V/A \tag{12}$$

and the total fragment number

$$N = A^3/V^2. \tag{13}$$

The above procedure was used to analyze the majority of the fragment debris radiographs in the present study and extract experimental fragment size and number data.

Nominal fragment size versus impact velocity for the same tests plotted in Fig. 9 is shown in Fig. 10. Each test in Fig. 10 is made independent of the experiment in the following way. First, a strain rate at failure is calculated by dividing the radial expansion velocity by the initial radius of the sphere, $\dot{\varepsilon} = V_e/R$. Second, a dynamic toughness is calculated based on the strain rate and the average fragment size from eqn (12) through the relation

$$K_f = \frac{\rho c \dot{\varepsilon} S^{3/2}}{\sqrt{24}}. \tag{14}$$

Equation (14), which relates the dynamic fragmentation toughness to fragment size and expansion strain rate, has been developed in an energy-based theory of dynamic fragmentation of solids (Grady, 1988). The property K_f provides a measure of the fracture resistance. Results for the same four experiments are shown in Fig. 11.

The dynamic toughness is also compared with the static critical stress intensity factor for this steel in Fig. 11. Although the data suggest a reduced toughness of the steel under the 10^4–10^5 s^{-1} strain rates of the dynamic fragmentation event, such a conclusion would

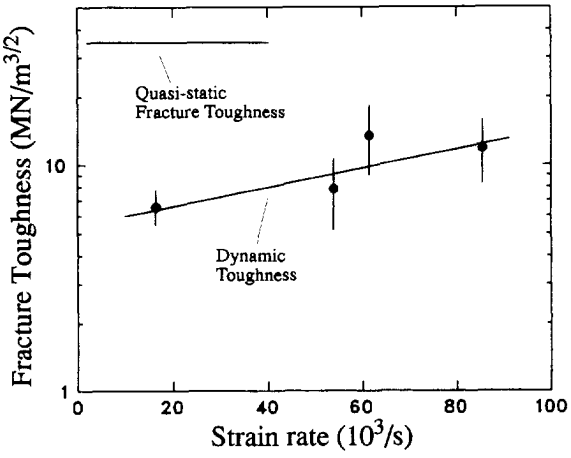

Fig. 11. Dynamic toughness data for E51200 steel (Fig. 9 data). Comparison with static fracture toughness data.

be premature at the present time because of the relatively early state of development of the fragmentation theory.

7. CONCLUSIONS

The resistance to, and the mechanisms of, catastrophic fragmentation of solids under intense impulsive loading have not been studied extensively. Current test techniques, which include Hopkinson bar methods and plate impact spall experiments, have so far not been sufficient to provide the property data needed to predict adequately such events. There is a need for alternative test methods to measure fragmentation properties and to compare the relative fragmentation resistance merits of different solids.

In this work a technique has been explored in which controlled impulsive loading, produced through ballistic impact methods, has led to dynamic deformation and fragmentation motions which may be sufficiently uniform, at least for engineering purposes, to yield useful material property data on failure and fragmentation behavior of solids. Data on the energy-to-failure and the dynamic fracture resistance for one steel have been determined to demonstrate the technique. Further investigation of additional materials will be required to validate the test method.

Acknowledgements—The authors wish to acknowledge the support of Ronald Moody and Randy Hickman in the performance of the impact and radiography experiments.

REFERENCES

Ang, J. A. (1990). Impact flash jet initiation phenomenology. *Int. J. Impact Engng* **10,** 23–33.
Backman, M. E. and Goldsmith, W. (1978). The mechanics of penetration of projectiles and targets. *Int. J. Engng Sci.* **16,** 1–99.
Brown, W. K. (1989). Fragmentation of the universe. *J. Astrophys. Astr.* **10,** 89–112.
Englman, R., Jaeger, Z. and Levi, A. (1984). Percolation theoretical treatment of two-dimensional fragmentation in solids. *Phil. Mag. B* **50,** 307–315.
Glenn, L. A. and Chudnovsky, A. (1986). Strain energy effects on dynamic fragmentation. *J. Appl. Phys.* **59,** 1379–1380.
Grady, D. E. (1982). Local inertia effects in dynamic fragmentation. *J. Appl. Phys.* **53,** 322–325.
Grady, D. E. (1988). The spall strength of condensed matter. *J. Mech. Phys. Solids* **36,** 353–384.
Grady, D. E. (1990). Particle size statistics in dynamic fragmentation. *J. Appl. Phys.* **68,** 6099–6105.
Grady, D. E. and Kipp, M. E. (1985). Geometric statistics and dynamic fragmentation. *J. Appl. Phys.* **58,** 1210–1222.
Johnson, G. R., Stryk, R. A., Holmquist, T. J. and Souka, O. A. (1990). Recent EPIC code developments for high velocity impact: 3D element arrangements and 2D fragment distributions. *Int. J. Impact Engng* **10,** 281–294.
Johnson, W. A. and Mehl, R. F. (1939). Reaction kinetics in processes of nucleation and growth. *Trans. AIMME* **135,** 416–458.
Kipp, M. E. (1993). Target response to debris cloud incidence. *Proceedings of the American Physical Society Topical Group on Shock Compression of Condensed Matter Conference*. Colorado Springs, Colorado, 28 June–2 July 1993, pp. 1849–1852.
Kipp, M. E. and Grady, D. E. (1985). Dynamic fracture growth and interaction in one dimension. *J. Mech. Phys. Solids* **33,** 399–415.
Kipp, M. E., Grady, D. E. and Swegle, J. W. (1993). Experimental and numerical studies of high-velocity impact fragmentation. Sandia National Laboratories Technical Report SAND93-0773, August.
Melosh, H. J., Ryan, E. V. and Asphaug, E. (1992). Dynamic fragmentation in impacts: hydrocode simulation of laboratory impacts. *J. Geophys. Res.—Planets* **97,** 14735–14759.
Smith, V. (1989). Kaman Sciences Corporation. Personal communication.